Monthly Notices
of the
ROYAL ASTRONOMICAL SOCIETY

Mon. Not. R. Astron. Soc. **411,** 411–421 (2011) doi:10.1111/j.1365-2966.2010.17693.x

Detection of optical coronal emission from 10^6-K gas in the core of the Centaurus cluster

R. E. A. Canning,[1⋆] A. C. Fabian,[1] R. M. Johnstone,[1] J. S. Sanders,[1] C. S. Crawford,[1] N. A. Hatch[2] and G. J. Ferland[3]

[1] *Institute of Astronomy, Madingley Road, Cambridge CB3 0HA*
[2] *School of Physics & Astronomy, University of Nottingham, Nottingham NG7 2RD*
[3] *Department of Physics, University of Kentucky, Lexington, KY 40506, USA*

Accepted 2010 September 10. Received 2010 September 7; in original form 2010 July 21

ABSTRACT

We report a detection ($3.5 \times 10^{37} \pm 5.6 \times 10^{36}$ erg s^{-1}) of the optical coronal emission line [Fe x] λ6374 and upper limits of four other coronal lines using high-resolution VIMOS spectra centred on NGC 4696, the brightest cluster galaxy in the Centaurus cluster. Emission from these lines is indicative of gas at temperatures between $1 \times 10^6 - 5 \times 10^6$ K, so traces the interstellar gas in NGC 4696. The rate of cooling derived from the upper limits is consistent with the cooling rate from X-ray observations ($\sim$10 M$_\odot$ yr^{-1}); however, we detect twice the luminosity expected for [Fe x] λ6374 emission, at 10^6 K, our lowest temperature probe. We suggest this emission is due to the gas being heated rather than cooling out of the intracluster medium. We detect no coronal lines from [Ca xv], which are expected from the 5×10^6 K gas seen near the centre in X-rays with *Chandra*. Calcium is, however, likely to be depleted from the gas phase on to dust grains in the central regions of NGC 4696.

Key words: galaxies: clusters: individual: Centaurus – galaxies: clusters: intracluster medium.

1 INTRODUCTION

The X-ray-emitting gas at the centres of clusters of galaxies can have very short cooling times. Without a heating source, this gas should cool and condense at rates of up to thousands of solar masses per year. However, high-resolution X-ray spectroscopy has been unable to detect large quantities of gas cooling below one-third of the cluster virial temperature (for a review, see Peterson & Fabian 2006). Observed rates of star formation and quantities of cool and cold gas in brightest cluster galaxies (BCGs), the most massive galaxies known, are far lower than expected (see e.g. McNamara et al. 2006). For the hot gas to be radiating but not cooling in the predicted quantities, a heating mechanism is required.

To determine how the heating and cooling balance in clusters of galaxies is maintained requires a multiwavelength approach to probe the many phases of matter. The hot intracluster medium (ICM), seen in X-rays, is at a temperature of $\sim 10^7$–10^8 K. Cool, optical emission-line gas, found to surround the majority of BCGs in cool core clusters, is seen at temperatures of $\sim 10^4$ K. Cold molecular gas reservoirs have also been observed; however, observations of gas at intermediate temperatures (10^5–10^6 K) have thus far proved elusive.

High-ionization, collisionally excited optical coronal lines are emitted at temperatures between 10^5–10^6 K making them important tracers of intermediate-temperature gas. Optical emission lines have the advantage of being observable from the ground. The high spectral and spatial resolution, in principle, allows us to determine and trace the velocity structure, and therefore examine the transport processes, in the gas. Emission lines from these plasmas can also provide a direct means of measuring the mass flow rate (Cowie 1981) and therefore the rate at which the ICM is condensing. Graney & Sarazin (1990), Sarazin & Graney (1991) and Voit, Donahue & Slavin (1994) have modelled coronal line emission in conditions appropriate to those of the cores of galaxy clusters.

There have been several attempts to detect coronal line emission from cooling gas in clusters of galaxies; however, reports of a significant detection remain inconclusive. Hu, Cowie & Wang (1985) observed the core regions of 14 clusters of galaxies, but were unable to detect the presence of [Fe XIV] λ5303 in any of their long-slit spectra. Similarly. Heckman et al. (1989) attempted detection of another coronal line, [Fe x] λ6374, in a sample of nine suspected 'cooling flow' clusters. Likewise, they found no detectable emission.

The first reported detection of coronal emission was by Anton, Wagner & Appenzeller (1991) in Abell 1795. The authors claimed to have found a 13σ detection of the [Fe x] λ6374 line in the core of the cluster with an aperture centred on the central 2 arcsec of the

⋆E-mail: bcanning@ast.cam.ac.uk

cD galaxy. A later study of the same object by Donahue & Stocke (1994) failed to confirm this detection. The sample used by Donahue & Stocke (1994) contained five massive cool core clusters and in the same paper, they report three more non-detections (A2199, 2A0335+096 and A2597) and one marginal (3σ) detection in PKS 0745−191. This detection has also failed to be confirmed in a later study by Yan & Cohen (1995).

The emission-line nebulosities around NGC 1275, the BCG in the Perseus cluster, were studied by Shields & Filippenko (1992). They searched for [Fe x] λ6374 emission in off-nuclear regions, away from the central active galactic nucleus (AGN), but also obtained no detection.

Up until now the two most recent searches for coronal line emission have been by Yan & Cohen (1995) and Sabra, Shields & Filippenko (2000). Yan & Cohen (1995) searched for emission from [Fe x] λ6374 in Abell 1795 and PKS 0745−191, the only two clusters where detections of coronal line emission had previously been reported. Contrary to these results, they did not find any significant detection in either cluster, but were able to place upper limits on the surface brightness by a factor of 10 deeper.

In a larger programme studying the properties of the emission-line nebulosity in NGC 1275, Sabra et al. (2000) searched for coronal lines over a wide wavelength range using Keck. Six coronal line transitions were covered in this range from [Ni XII] λ4232 to [Ni XII] λ6702. No coronal line emission was seen in their data.

This work reports on deep, high spectral resolution, integral field spectroscopy (IFS) observations of NGC 4696 (RA $12^{h}48^{m}49^{s}$, Dec. $-41^{\circ}18'40''$ J2000), the BCG in the Centaurus cluster (Abell 3526). The Centaurus cluster at redshift $z = 0.0104$ is the second nearest example of a cool core cluster. The heating and cooling in this cluster is apparently very well balanced, despite the short central cooling time of only 200 Myr. NGC 4696 houses a radio source and multiple bubbles. These are accompanied by soft X-ray filaments and a sharp rise in the metal abundance in the central 30 kpc, among the highest seen in any cluster, approximately twice solar (Sanders & Fabian 2002; Fabian et al. 2005; Sanders & Fabian 2006a). The Centaurus cluster also has the broadest range of X-ray temperatures seen, containing gas from 0.35 to 3.7 keV, over a factor of 10 in temperature (Sanders et al. 2008).

Crawford et al. (2005) presented images showing the extensive, filamentary Hα nebulosity surrounding NGC 4696. These share the morphology of the soft X-ray filaments and of a prominent dust lane (Sparks, Macchetto & Golombek 1989). The low X-ray temperatures, short cooling times and exceptionally high metallicities in this nearby cluster make it the ideal target for a deep search for coronal line emission.

The observations are briefly described in Section 2, method, analysis and limits on coronal line emission are given in Section 3 and in Section 4, we discuss the implications of these limits. We summarize our results and main conclusions in Section 5. At the redshift of the Centaurus cluster ($z = 0.0104$, 44.3 Mpc), 1 arcsec corresponds to 0.210 kpc (throughout this paper, we adopt $H_0 = 71\ \mathrm{km\ s^{-1}\ Mpc^{-1}}$, $\Omega_{\mathrm{M}} = 0.27$ and $\Omega_{\Lambda} = 0.73$). Abundances given in this paper are relative to the solar metallicities of Anders & Grevesse (1989).

2 OBSERVATIONS AND DATA REDUCTION

Observations were made on 2009 March 27–30 using the VIsible MultiObject Spectrograph (VIMOS) on the VLT in La Paranal, Chile (see LeFevre et al. 2003 and Zanichelli et al. 2005 for a description of the VIMOS IFU and a discussion of data reduction techniques). We obtained High Resolution Orange (HRO) data using the VIMOS Integral Field Unit (IFU). We used the larger 0.67-arcsec fibres giving a field of view of 27×27 arcsec^2 with the HRO grism.

We acquired 10.5-h exposure centred on the inner region of NGC 4696($12^{h}48^{m}49^{s}.3$, $-41^{\circ}18'40''$), the deepest observations thus far to try to detect emission from cooling hot gas in these objects. We also took six 15-min exposures using the same setup to image the entire galaxy including many sky fibres.

The data were reduced by the VIPGI[1] pipeline (see Scodeggio et al. 2005 for a description of VIPGI). The 3D data cubes were combined and analysed with a set of IDL routines (R. Sharp, private communication).

Instrument flexures in VIMOS are very dependent on the rotator position and suffer from hysteresis (Amico et al. 2008). For this reason, we took calibration frames after each observation block.

Cosmic-ray rejection, final fibre-to-fibre transmission corrections, sky subtraction, correction for Galactic extinction and shifting to the object rest frame were performed outside VIPGI using IDL routines. The data reduction procedure will be explained thoroughly in a forthcoming paper, Canning et al. (in preparation), detailing observations of the emission-line nebulae surrounding NGC 4696.

3 METHOD, ANALYSIS, DETECTIONS AND LIMITS

Our HRO spectra cover the wavelengths of a number of coronal lines, specifically [Fe XIV] λ5303, [Ca XV] λ5445, [Ca XV] λ5694, [Fe x] λ6374 and [Ni XV] λ6702.

The expected location of the [Fe x] λ6374 feature coincides with the red-wing of the [O I] λ6363 object emission, so requires special attention (see Section 3.2). None of our other expected coronal lines coincide with object emission lines or sky lines.

3.1 Continuum subtraction

When determining flux from possibly broad and faint emission lines, errors in continuum subtraction are likely to dominate. For this reason, continuum subtraction was attempted in a number of ways. The first method we employ is to use a small sample of fibres from within the galaxy, in a region where no significant coronal emission is seen. A second method is to subtract a smoothed continuum from the spectra (as in Donahue & Stocke 1994) and finally we model the continuum with simple stellar population (SSP) models from Bruzual & Charlot (2003) (hereinafter referred to as BC03). These methods are described below:

(i) In an initial search, where we binned the spectra based on the X-ray temperature, the lowest temperature regions (box 1 and 2, Fig. 1) overlap with the temperature range at which some coronal lines are emitted, specifically the lines of [Ca XV] (5×10^6 K). In box 1, we found evidence for a flux excess on the red-wing of the [O I] λ6363 emission line, blueshifted slightly from 6374 Å, where we would expect [Fe x] λ6374. We found no significant excess in box 2. We then use the spectrum of box 2 to correct the continuum of box 1 and search for significant flux excess in regions of expected coronal emission.

(ii) A smooth continuum is fitted to the sky-subtracted spectra with all regions, where emission lines are expected, and regions of poor sky subtraction masked out. The smooth continuum is then subtracted from those spectra.

[1] VIPGI – VIMOS Interactive Pipeline Graphical Interface obtained from http://cosmos.iasf-milano.inaf.it/pandora/.

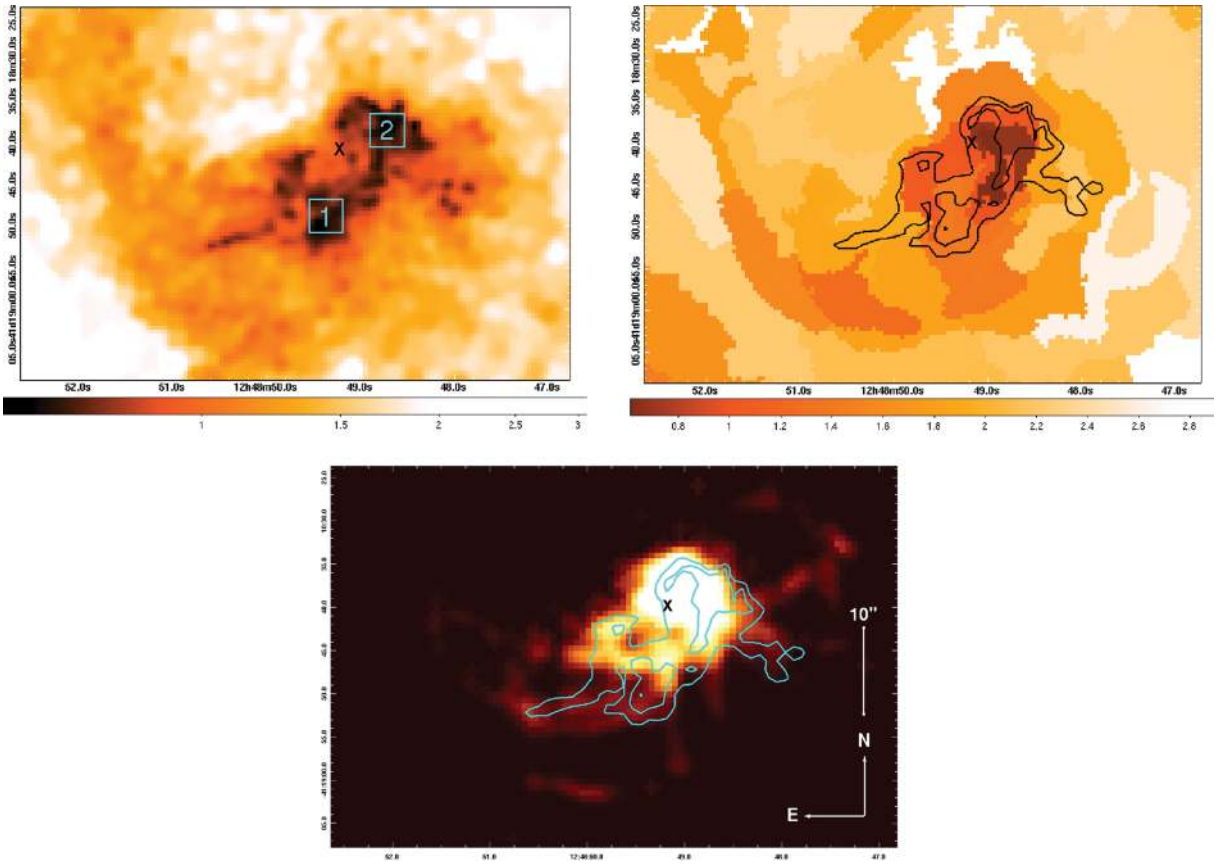

Figure 1. Top left-hand panel: X-ray temperature map of the centre of the Centaurus cluster (Fabian et al. 2005). The colour bar is in units of keV. Boxes 1 and 2 are situated at the regions of the lowest X-ray temperature. Top right-hand panel: X-ray metallicity map based on Fe abundance. The colour bar is in units of solar metallicity. The 0.4–0.8 keV X-ray temperature contours are overlaid. Bottom panels: [N II] λ6583 emission in NGC 4696 overlaid with X-ray contours of 0.4–0.8 keV gas. All images are on the same scale (10 arcsec = 2.1 kpc). The black X indicates the centre of the radio emission. Box 1 is at the position RA $12^{h}48^{m}49\overset{s}{.}4$, Dec. $-41^{\circ}18'48\overset{''}{.}9$ (J2000) and box 2 is situated at RA $12^{h}48^{m}48\overset{s}{.}7$, Dec. $-41^{\circ}18'38\overset{''}{.}6$ (J2000). Both boxes are 5 by 5 fibres large corresponding to 3.4 arcsec (0.7 kpc) across.

(iii) The continuum shape is fitted using the STARLIGHT software (Cid Fernandes et al. 2005, 2009) and basefiles made up of 240 BC03 models spanning six metallicities, covering the range 0.005–2.5 $Z_{\odot}$, and 40 ages, covering the range 0–20 Gyr. Using this software requires that we re-grid our spectra to integer wavelengths. STARLIGHT uses a Markov Chain approach to fit the data. We determine the parameters to use by fitting the data many times and looking at the distribution of fits over the region of interest. The fit with the best χ^2 value is taken as the continuum and subtracted from the spectrum. An example of a fit with emission lines masked out is shown in Fig. 2. STARLIGHT does not allow us to examine the uncertainty in the parameters from a fit and so we use a Monte Carlo approach to determine the error. We quantify the additional uncertainty introduced due to the continuum subtraction by perturbing our data points by a Gaussian random number with mean and variance given by the data and associated Poisson error. These new perturbed spectra are then fitted with the STARLIGHT software using the same parameters as before. We repeat this 200 times for our box 1 spectrum; the range of fits over the [Fe X] λ6374 region can be seen in the top panel of Fig. 3. The lower panel of Fig. 3 shows the distribution of the integrated flux (counts model) over the wavelength region 6355–6380 Å. The Gaussian shape of this distribution implies that we have repeated the fits enough number of times to properly sample the range of models, which could provide a good fit to the data. The 200 model continua are then re-gridded to the same

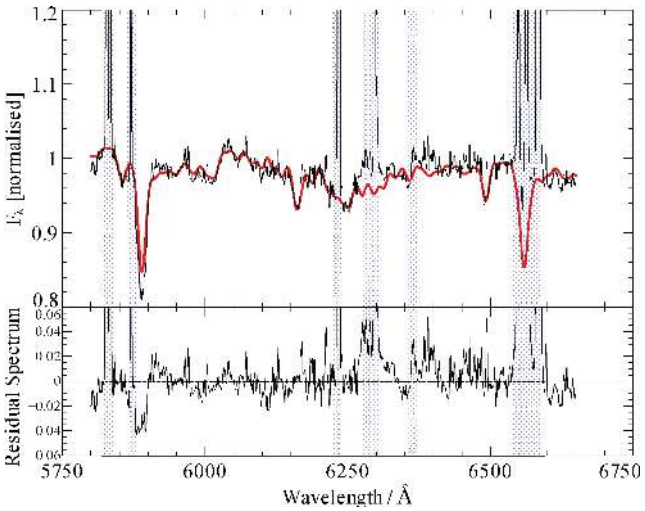

Figure 2. The best-fitting BC03 SSP model (red) to the observed spectrum, from box 1 (black), between 5700–6700 Å and the fit residuals. Regions where we expect object emission lines and regions of poor sky subtraction were masked out in the fit and are shown above in grey.

wavelength grid as our original data. We estimate the additional uncertainty in each spaxel as the 1σ deviation in the range of models. This uncertainty is dependent on the error spectrum of the entire

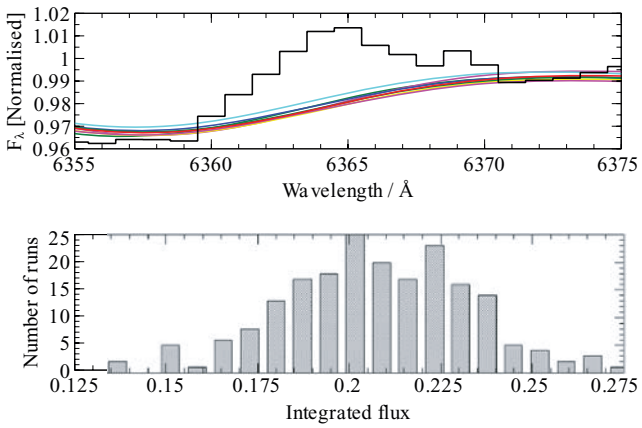

Figure 3. Top panel: the range of STARLIGHT fits over the [Fe X] λ6374 region, in box 1, determined by perturbing and re-fitting the observed spectrum. Bottom panel: the distribution of integrated flux values for 200 STARLIGHT fits over the [Fe X] λ6374 region.

wavelength range of the spectra being fitted and as such will only be weakly correlated with the Poissonian error on each spaxel. We therefore estimate the total uncertainty as the quadrature addition of the Poissonian error and the uncertainty in the continuum model.

An advantage of using synthetic spectra for the continuum subtraction is that we can ensure that there is no coronal line emission in the fit, so we are not subtracting any signal. The stellar spectra are much more complicated than a smoothed profile and we would like to test whether any apparent excess flux found, where we would expect coronal line emission could be due to a 'bump' in the stellar spectra. However, the spectral models assume that the relative abundances are the same, which may not be appropriate to NGC 4696. The stellar continuum will also vary across the field, and in binning spectra over a large region of the galaxy, we would expect the SSP model fit to deteriorate. For these regions, fits were run separately on all spectra, that is, we did not use the best-fitting STARLIGHT model of box 1 to correct for the stellar continuum of any spectra other than box 1.

3.2 [Fe X] λ6374

The [Fe X] λ6374 coronal emission feature coincides with the red-wing of the [O I] λ6363 emission and as such warrants special treatment (see Fig. 5 shown later). Unfortunately, the object [O I] λ6300 emission also coincides with the sky [O I] λ6363 emission feature.

We simultaneously fit Gaussians to the lines of [O I], the [N II] doublet, the [S II] doublet, Hα and the [Fe X] emission lines. This is in order to allow for the errors in scaling and removing the [O I] λ6363 object emission line. A single Gaussian component for each emission line gives a good fit in the regions of boxes 1 and 2 (see the upper panel of Fig. 4).

We tie the redshift and velocity width of the object optical emission-line nebulae ([N II] doublet, [S II] doublet and Hα and [O I]) emission lines. The redshift and velocity width of the sky [O I] lines are also tied. The integrated flux of the [N II] doublet and that of the two [O I] lines can be tied to each other, the scaling in each case being dictated by atomic parameters (Osterbrock & Ferland 2006). The integrated flux of the [Fe X] λ6374 emission line is fixed to be a positive value, but the redshift and velocity width are allowed to be free in the fit as there is no evidence yet for a spatial correspondence between the optical nebulosity and any coronal line emitting plasma. The continuum level for each line is fitted in a region local to the emission line. An example of the fitting process with the fit to the object [O I] emission lines and the [Fe X] λ6374 emission line is shown in Fig. 5.

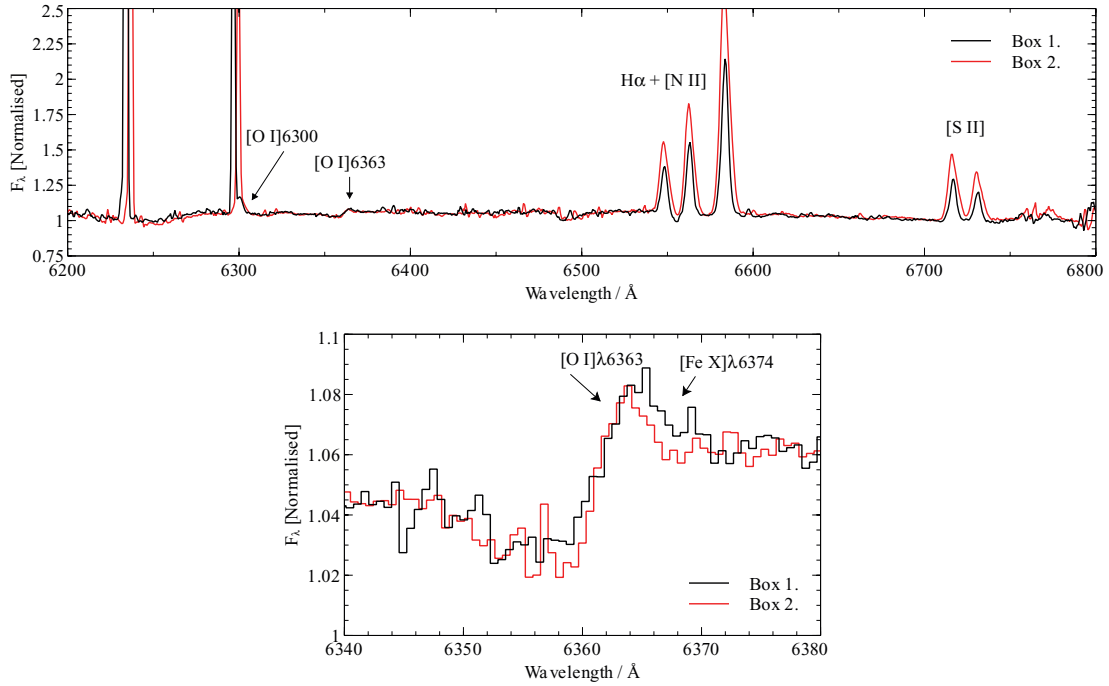

Figure 4. Top panel: spectra from box 1 (black) and box 2 (red) without continuum subtraction. All sky lines except [O I] λ6300 and [O I] λ6363 sky emission have been subtracted in order to more clearly see object emission-line features. Bottom panel: a blow-up of the expected [Fe X] λ6374 region. Emission from cool gas in box 2 has a broader velocity width than box 1 in general, except over the [O I] λ6363 and [Fe X] λ6374 regions. This demonstrates the excess flux on the red-wing of oxygen emission in box 1. This cannot be accounted for by subtraction of a template from the object [O I] λ6300 emission line.

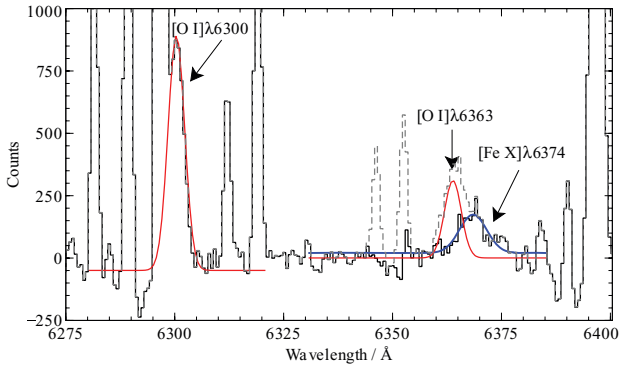

Figure 5. Spectrum from box 1, after subtraction of a smooth continuum, showing the fit to the [O I] λ6300 object emission line and the scaled template for the [O I] λ6363 emission (red). The blue Gaussian is the result of a fit to the remaining excess flux after subtraction of the oxygen line. The dashed spectrum is the original continuum-subtracted data and the solid line shows the effect of the [O I] λ6363 line subtraction. Here also two neighbouring sky lines are fitted and subtracted. The continuum is allowed to vary from zero and is fitted locally around the emission lines of interest.

3.3 Detections and upper limits

After continuum subtraction, detections and upper limits are established by fitting a Gaussian line profile to the spectra using MPFIT (Moré 1978; Markwardt 2009). The 90 per cent flux limits are found by increasing the integrated flux in the fit until $\Delta\chi^2$ has grown by 2.7; these results are presented in columns 2–4 of Table 1 and 2. The last three columns show, for two cooling rates and metallicities, the predicted luminosity of the coronal lines, assuming that they are the product of cooling from the hot ICM (see Sarazin & Graney 1991). During the fit, we fix the Gaussian normalization to be positive. When determining the upper limits, we also constrain the redshift and velocity width to be the same as that of the [Fe x] λ6374 emission line. The coronal lines probe a broad range of temperatures, so it is perhaps not obvious that they should have an identical velocity. The continuum is fitted in a region local to the emission lines.

We report a 6.3σ detection of excess flux at the expected wavelength of [Fe x] λ6374 emission in a region 15 arcsec away from the nucleus (box 1, Fig. 1). The quoted significance of this feature is from a fit to the SSP model continuum-subtracted spectrum. This method of continuum subtraction gave the least-significant result. We do not see any evidence of this emission in a region of the galaxy where there is similar low temperature X-ray gas nearer to the core (box 2). Fig. 4 shows a comparison of the spectra in these two regions. The velocity width of the cool (10^4 K) gas near the core is larger than that of the gas farther away in all cases, except the region around the [O I] λ6363 object emission. Here the box 1 spectra show an excess of flux towards the red-wing of the oxygen line; this is not seen in the box 2 spectra or in the line profile of the [O I] λ6300 line in box 1.

Fig. 6 shows the sky spectrum. This spectrum is formed from regions at the edge of the field of view, where we have no detectable object emission. The regions, where we would expect object [O I] λ6300, [O I] λ6363 and [Fe x] λ6374 emission, are indicated. There is no obvious sky emission in the region around the [O I] λ6363 and [Fe x] λ6374 lines and as the excess flux is seen as a very broad feature and it is not seen everywhere in the spectra, it is unlikely to be a confusion due to sky emission.

To fit the excess flux requires a redshift different from that of the optical emission-line nebulae, the line in box 1 is blueshifted with respect to the optical nebulosity. The line-of-sight velocity difference between the redshift of the Hα nebulae and the best fits to the excess flux is $\sim$230 km s^{-1}. This is comparable to the spread of the line-of-sight velocities in the optical nebulosity itself. The results from the three methods of continuum subtraction agree within the error (see Fig. 7). In box 1, the integrated flux with subtraction of the continuum using a region where no significant

Table 1. The 90 per cent (2.7σ) upper limits on the luminosity and detections of [Fe x] λ6374 emission with 1σ errors in the regions specified. The luminosity quoted as detections used the continuum-subtraction technique, which gave the lowest integrated flux; in all cases, this was when using the SSP model fits. Where the results are upper limits and not clear detections, the continuum-subtraction method yielding the largest integrated flux was taken. The model approximate luminosities are from Sarazin & Graney (1991) and scale simply with the cooling rate. Here they are given for a cooling rate of 3 (columns 5 and 6) and 10 $M_\odot$ yr^{-1} (column 7). These limits are determined by spectral fitting of the X-ray spectrum (Sanders et al. 2008). The sizes of the regions in arcsec^2 (kpc) are ^{a}3.4 arcsec^2 (0.7 kpc^2) and ^{b}20.1 arcsec^2 (4.2 kpc^2). These limits have been corrected for galactic extinction, but not for the intrinsic reddening of NGC 4696. The upper limits on [Ca xv] λ5694 imply that this is deficient by a factor of 2 in the inner 20 arcsec compared with the luminosity predicted from the X-ray cooling rate within this region.

Line	Luminosity (erg s^{-1})			Model (erg s^{-1})		
	Box 1^a (10^{37})	Box 2^a (10^{37})	20 arcsec^{2b} (10^{37})	$Z = Z_\odot$ (10^{37})	$Z = 0.5\,Z_\odot$ (10^{37})	$Z = Z_\odot$ (10^{37})
[Fe XIV] λ5303	<4.5	<4.0	<11.5	3.1	3.1	10.3
[Ca xv] λ5445	<1.0	<0.9	<9.1	1.4	1.2	4.7
[Ca xv] λ5694	<3.8	<1.4	<3.2	2.1	1.8	7.0
[Fe x] λ6374	3.5 ± 0.56	<7.0	25.8 ± 8.3	4.1	4.2	13.7
[Ni xv] λ6702	<1.1	<0.2	<1.7	0.2	0.2	0.6

Table 2. Same as columns 1–4 of Table 1 in units of flux.

Line	Flux (erg cm^{-2} s^{-1})		
	Box 1^a	Box 2^a	All pixels^b
[Fe XIV] λ5303	$<1.9 \times 10^{-16}$	$<1.7 \times 10^{-16}$	$<4.9 \times 10^{-16}$
[Ca xv] λ5445	$<4.4 \times 10^{-17}$	$<3.7 \times 10^{-17}$	$<3.9 \times 10^{-16}$
[Ca xv] λ5694	$<1.6 \times 10^{-16}$	$<5.9 \times 10^{-17}$	$<1.4 \times 10^{-16}$
[Fe x] λ6374	$1.5 \times 10^{-16} \pm 2.4 \times 10^{-17}$	$<3.0 \times 10^{-16}$	$1.1 \times 10^{-15} \pm 3.5 \times 10^{-16}$
[Ni xv] λ6702	$<4.6 \times 10^{-17}$	$<6.6 \times 10^{-18}$	$<6.0 \times 10^{-17}$

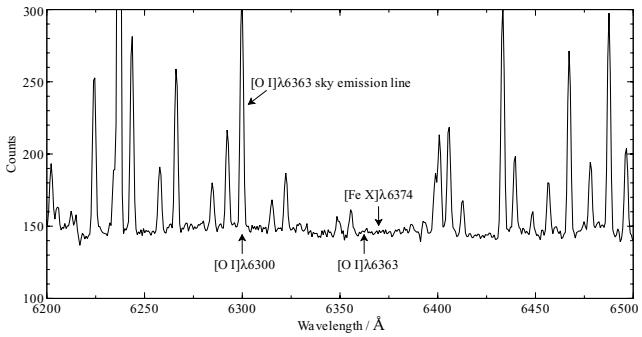

Figure 6. The sky spectra extracted from fibres at the edge of the field ∼35 arcsec from the centre of NGC 4696. The [O I] λ6363 sky emission line is labelled as are the regions where we would expect the object [O I] emission lines and the [Fe X] emission. The spectrum has been shifted to the rest wavelength of NGC 4696.

excess flux is observed, after subtraction of the [O I] λ6363 line, gives an integrated flux of $1.8 \times 10^{-16} \pm 2 \times 10^{-17}$ erg cm^{-2} s^{-1}, subtraction of a smoothed continuum gives an integrated flux in the line of $1.6 \times 10^{-16} \pm 2 \times 10^{-17}$ erg cm^{-2} s^{-1}; in both these cases, the error is determined from the Poissonian error in the spectrum, which is similar to the 1σ deviation after continuum subtraction of a nearby emission-free region of the spectrum, and finally SSP model fitting gives $1.5 \times 10^{-16} \pm 2.4 \times 10^{-17}$ erg cm^{-2} s^{-1}, including both the Poissonian error and the additional error in the continuum fit. Fig. 8 shows, for comparison, the same region with the template [O I] λ6363 line subtracted. There is no significant excess emission seen to the red-wing of the [O I] λ6363 line.

In regions containing strong stellar continuum features, where the background spectrum is highly structured ($\lambda < 6000$ Å), the error after continuum subtraction is larger than the simple Poissonian error.

The noise features in these regions have a width similar to the emission feature we are looking for (10–20 Å, see Fig. 9). We estimate the noise in these regions in two ways. First, we calculate the 1σ deviation from zero in an emission-free region of the spectrum (after continuum subtraction) on the scale of the variations in the continuum. Secondly, we fit a Gaussian of fixed width equal to the variations in the continuum. We then step the Gaussian over the emission-line-free region pixel by pixel. Due to the fluctuations in the noise, the Gaussian fit will sometimes have a positive normalization and sometimes a negative one. The distribution of the Gaussian area values in this region provides a second mechanism for estimating the 1σ uncertainty. The errors determined in both fashions were consistent with each other. Fig. 10 shows the upper limits overplotted on the continuum-subtracted spectrum for the [Fe XIV] λ5303, [Ca XV] λ5445, [Ca XV] λ5694 and [Ni XV] λ6702 lines.

3.4 Spatial distribution of the hot gas

The detection of [Fe X] λ6374 emission in box 1, but not in box 2, implies that there may be some 'clumpiness' to the spatial distribution of the intermediate-temperature gas. A small change in temperature equates to a vast change in emissivity (see Ferland et al., in preparation), so this clumpy appearance may be indicative of small variations in the temperature of the gas across the field of view.

Using IFS observations, we can trace the morphology of the regions, where there appears to be an excess of flux towards the red-wing of the [O I] λ6363 line. Fig. 11 shows the spatial distribution of

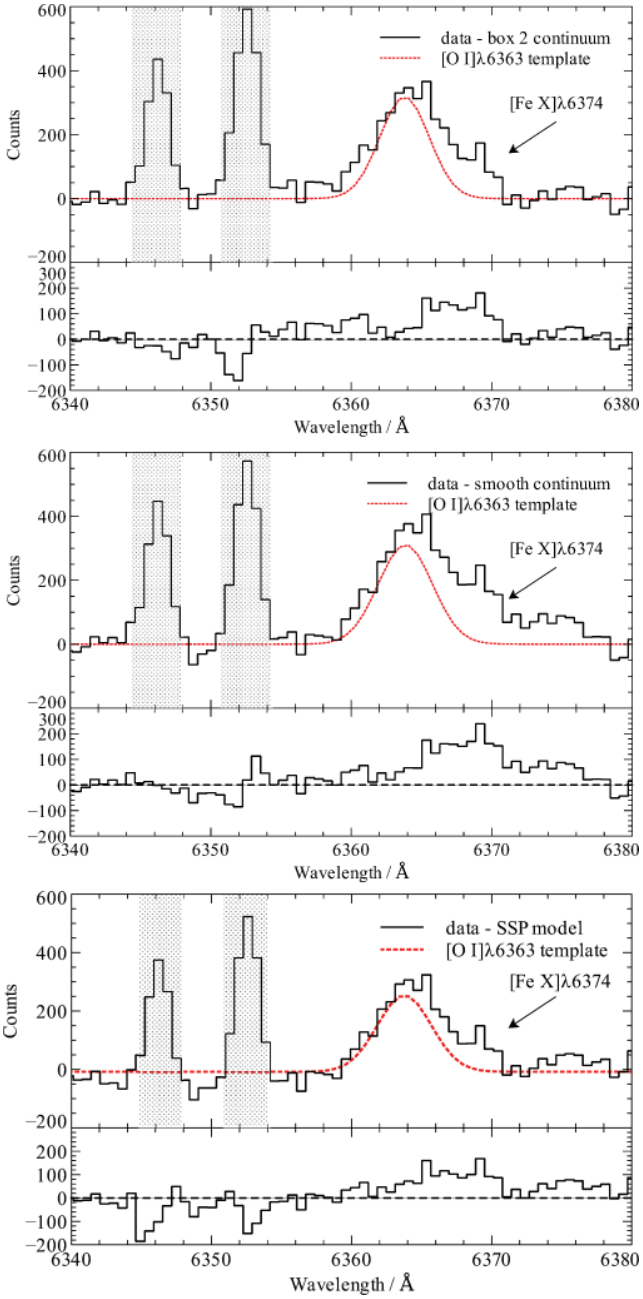

Figure 7. Top panel: box 1 spectra after continuum subtraction using the continuum from box 2 spectra. Middle panel: box 1 spectra with smooth continuum subtracted. Bottom panel: box 1 spectra with best-fitting STARLIGHT continuum model subtracted. In each plot, the top panel shows the data over the wavelength region containing the [O I] λ6363 object emission and probable [Fe X] λ6374 object emission. The red line shows the scaled [O I] λ6300 emission used as a template to subtract the contribution of the [O I] λ6363 line. The bottom panel, in each case, shows the residuals from a subtraction of the [O I] λ6363 template. In each plot, an excess of flux can be seen around a wavelength of 6368 Å. The two emission lines that have been greyed out, to the left-hand side of the [O I] λ6363 line, are sky lines. These were fitted and subtracted from the spectrum before a fit to the remaining excess flux was performed.

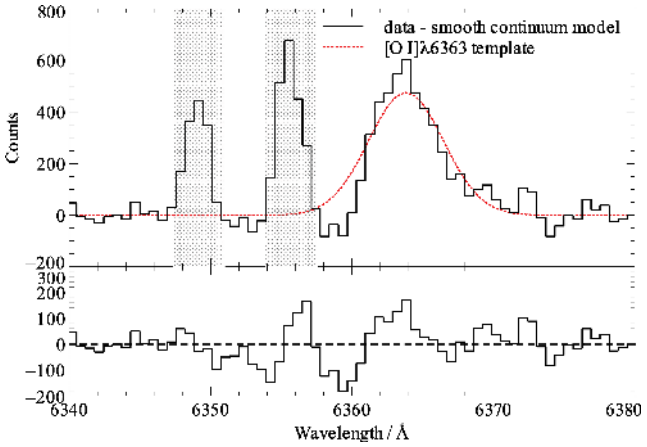

Figure 8. Box 2 spectrum with a smooth continuum subtracted. There is no significant excess emission seen on the red-wing of the object [O I] λ6363 emission line.

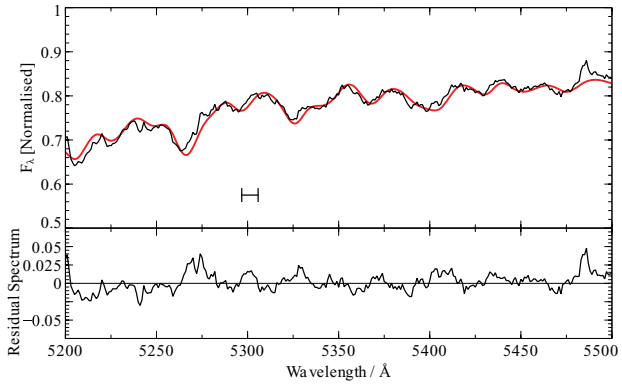

Figure 9. The STARLIGHT fit in the bluest region of our spectra. After subtraction of the model stellar continuum, we are left with variations in the residual spectrum on the scale of 10–20 Å. This is comparable to the width of the feature we find on the red-wing of the [O I] λ6363 object emission line. For comparison, the line shows the $\pm 1\sigma$ width of a 475 km s^{-1} FWHM velocity width line at the rest wavelength of the [Fe XIV] λ5303 coronal emission line.

this excess flux across the field of view, overlaid with the contours of radio emission (see Taylor et al. 2007). We binned the spectra in 5 by 5 regions; this size-binning was used as a compromise between spatial resolution, signal-to-noise ratio and goodness of fit to the stellar continuum. We then fit each region with SSP models as described in Section 3.1. The [O I] λ6363 object emission line was then fitted and removed and the remaining 'counts' between 6363–6380 Å were summed (no emission_line shape was assumed here) to create the map of relative flux, seen in the bottom panel of Fig. 11. As an illustration, we show, in Fig. 12, spectra from bin A and B, the regions of highest excess flux, and spectra from bin C and D, where little excess flux is seen.

3.5 Velocity of the hot gas

Assuming a Gaussian profile for the [Fe X] λ6374 emission line detected in box 1, we can fit the velocity width of the detected broad excess flux. We do this for each of the methods of continuum subtraction, as described above. The full width at half-maximum (FWHM) velocity width of the feature determined from the different continuum-subtraction methods is 300–650 km s^{-1} from box 1 (the velocity width of [O I] λ6363 is ∼200 km s^{-1}). It should be noted that the predicted integrated line profile of the coronal line emission is model-dependent (Sarazin & Graney 1991); however, our data are not deep enough to allow for an investigation of the line profile. The thermal linewidth of the coronal line emission is typically only 20–30 km s^{-1}, so the broad width of this feature is likely due to turbulent motions of the hot gas. Sarazin & Graney (1991) show that for a gas of 2×10^6 K with maximal turbulent broadening (velocities limited by the sound speed in the hot ambient medium), predicted velocity widths at FWHM are approximately 1700 km s^{-1}. The motions in the gas we observe are therefore highly subsonic.

4 DISCUSSION

We have conducted a deep search for five species of optical coronal line emission, specifically [Fe XIV] λ5303, [Ca XV] λ5445, [Ca XV] λ5694, [Fe X] λ6374 and [Ni XV] λ6702. These lines probe gas at temperatures of 2×10^6, 5×10^6, 5×10^6, 1.3×10^6 and 2.5×10^6 K, respectively.

We report four upper limits and a 6.3σ detection of [Fe X] λ6374 emission. This detected feature is broader than the Hα nebulosity at 10^4 K, having an FWHM velocity width of about 300−650 km s^{-1} and is blueshifted with respect to this cooler emission. [Fe X] λ6374 is emitted from gas at 10^6 K, the lowest temperature of the coronal lines in our wavelength range.

Assuming that coronal line emission is a product of the low level of residual cooling out of the hot gas observed in the central galaxies of galaxy clusters, we can determine the rate of cooling from the flux of these lines. Upper limits for the detection of [Fe XIV] λ5303 and [Ni XV] λ6702 are consistent with the X-ray cooling rate, in the absence of heating, of ∼10 M$_\odot$ yr^{-1} (Sanders et al. 2008) above 0.8 keV, over a region 20 arcsec in diameter. However, in the case of [Fe XIV] λ5303, we stress the difficulties involved in the subtraction of the stellar continuum, which introduces a larger error into the detection limit (see section 3.1 and Fig. 9).

The rate of cooling implied by the detection of [Fe X] λ6374 emission is a rate of ∼20 M$_\odot$ yr^{-1} in the central 20 arcsec^2, twice that inferred from X-ray observations and from the upper limits of the other coronal lines (see Table 1 and 2). If this emission is solely due to the cooling of the ICM in this cluster, we would expect similar or greater detections from the [Fe XIV] λ5303 and [Ca XV] lines. An alternative for the iron emission is that it originates in gas, which was cooler and has been heated. There are lots of possible sources of heating, including shocks, photoionization from central AGNs, thermal conduction, turbulent mixing or heating associated with the radio bubbles. We caution that recent changes in the atomic parameters indicate that the emissivity of [Fe X] λ6374 is larger than previously thought. This would imply a slightly lower cooling rate than calculated here and will be investigated in further work by Ferland et al. (in preparation).

C IV 1549 Å emission has been discovered by Sparks et al. (2009) in the outer regions of M87, co-located with its Hα filaments. This probes the slightly lower temperatures of $\sim 10^5$ K. O VI 1032, 1035 Å emission ($\sim 10^{5.5}$ K) has also been seen in a small sample of cool core clusters (Oegerle et al. 2001; Bregman et al. 2006). Bregman et al. (2006) note that in Abell 1795, the cooling rate implied by the $10^{5.5}$ K is larger than that implied by the X-ray emission, as is the case here. They suggest that non-steady cooling of material may be the cause of this conflict.

Most AGNs show emission from forbidden, high-ionization lines, the so-called extended coronal line regions (CLRs) (Mullaney et al. 2009; Mazzalay, Rodríguez-Ardila & Komossa 2010). This emission is believed to be from a region outside the broad-line region

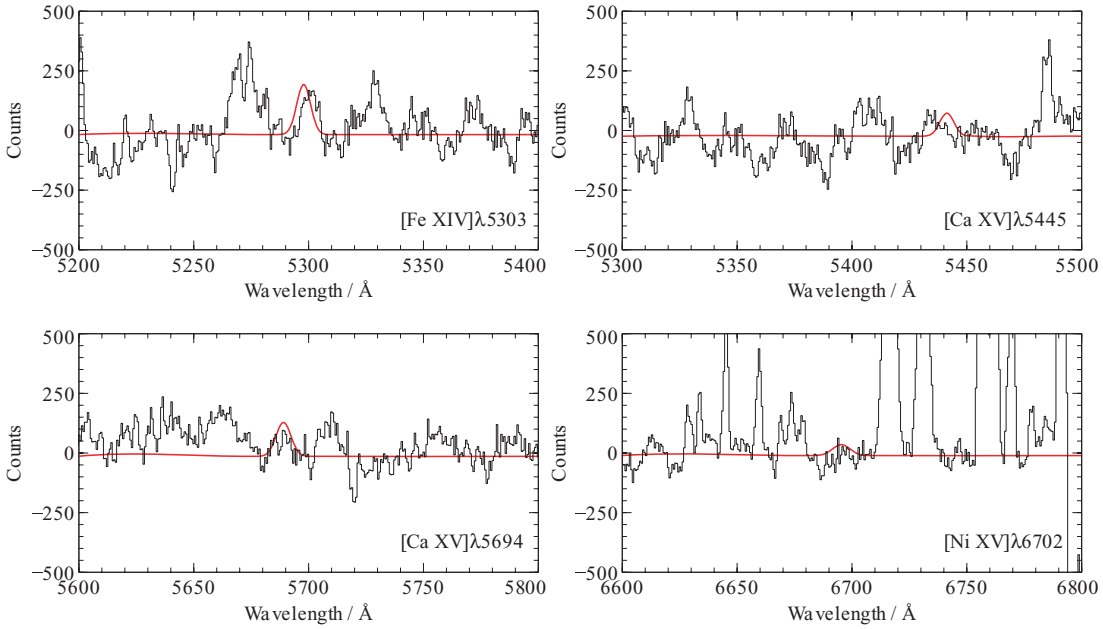

Figure 10. The 90 per cent upper limits overplotted on the continuum-subtracted spectra from box 1 for the lines of [Fe XIV] λ5303, [Ca XV] λ5445, [Ca XV] λ5694 and [Ni XV] λ6702. Here the continuum was subtracted using SSP models fitted with the STARLIGHT software package. The redshift and velocity width of the emission lines are constrained to be the same as that of the detected [Fe X] λ6374 line.

and inside the narrow-line region, and lines are often observed to be blueshifted by 500 or more km s^{-1}. Mazzalay et al. (2010) find that photoionization from the central AGN is likely to be the major ionization mechanism for these regions. Their results also confirm the observation that higher ionization lines are emitted from a more compact area, while the lower ionization lines can be found farther into the narrow-line region.

For a typical Seyfert galaxy with an ionizing luminosity $L_{\rm ion} = 10^{43.5}$ erg s^{-1}, Ferguson et al. (1997) find that the region containing [Fe X] λ6374 emission should be restricted to the inner 20 pc. The size of the CLR scales with the ionizing luminosity of the central source as $L_{\rm ion}^{1/2}$ (Ferguson et al. 1997). Box 1, where we find significant [Fe X] λ6374 emission, is located ∼15 arcsec from the centre of the radio source, a distance of ∼3 kpc. Scaling up from the values of Ferguson et al. (1997), a region of the size ∼3 kpc implies a huge ionizing luminosity of 10^{47} erg s^{-1}. Taylor et al. (2006) have found the nucleus of NGC 4696 to be very faint. Their upper limit on the luminosity from X-ray observations between 0.1–10 keV is $\sim 10^{40}$ erg s^{-1}. The spatial extent over which we find the coronal line emission leads us to rule out the possibility of photoionization by the central AGN. It is possible, looking at the residual flux over the spectral region where we would expect [Fe X] λ6374 emission, that the spatial distribution of the 10^6-K gas (Fig. 11) traces that of the 10^4-K filaments and large dust lane; however, this is a tentative result and would need confirmation with deeper observations.

Another explanation for the excess flux, such as emission from a merging clump of gas or another filament, is unlikely, as any extra component of [O I] λ6363 emission should also be present in the [O I] λ6300 emission and no red-wing is observed on this line. One explanation for the blueshift could be that the radio source is interacting with and driving the plasma away, possibly entraining with its cooler gas. Fig. 13 shows a two-component fit to the [N II] and Hα emission in the box 1 spectrum. There is evidence for a blueshifted component to these lines and the best-fitting Gaussians imply a blueshifted velocity of ∼140 km s^{-1}. This is less than the observed blueshift of the [Fe X] λ6374 line (∼230 km s^{-1}), so is inconclusive.

Sanders et al. (2008) have used deep *XMM–Newton* Reflection Grating Spectrometer (RGS) observations to show that the centre of the Centaurus cluster contains X-ray-emitting gas down to at least 4×10^6 K through detections of the Fe XVII line and limits on the O VII emission. The metal abundances are very high in the inner 30 kpc of this cluster (Sanders & Fabian 2006a). The iron abundance of the hot gas is approximately two times solar and the calcium abundance approximately three times solar. The *Chandra* spectra show evidence of an off-centre abundance peak at ∼20 kpc. The best-traced elements of Fe and Si then show a decline in abundance in the nucleus.

At these high abundance values, we expect to detect, in our optical spectra, lines of [Ca XV], probing gas of 5×10^6 K, detected already by its X-ray Fe XVII emission. Contrary to this expectation, we do not detect any significant calcium emission. Upper limits in most cases suggest that the rate of radiative cooling is less than that inferred from the X-ray spectra of hotter gas and provide a more stringent constraint than the other coronal emission lines.

We explore four possible explanations for this result: inaccurate continuum subtraction; a lower cooling rate; a low calcium abundance; and calcium deficiency in the intermediate-temperature gas. We will deal with each of these points in turn.

The continuum subtraction has been attempted in a variety of ways (see Section 3.1) and in all cases produces similar results. Where these results were upper limits and not clear detections, the largest value was taken and is given in Table 1. Where the stellar spectra exhibit many features, the uncertainties are large and the detection of broad line emission is very difficult. However, in the absence of a template spectrum in which we are sure that there is no emission from intermediate-temperature gas and observations with similar abundance ratios across the field of view, this is the best we can do.

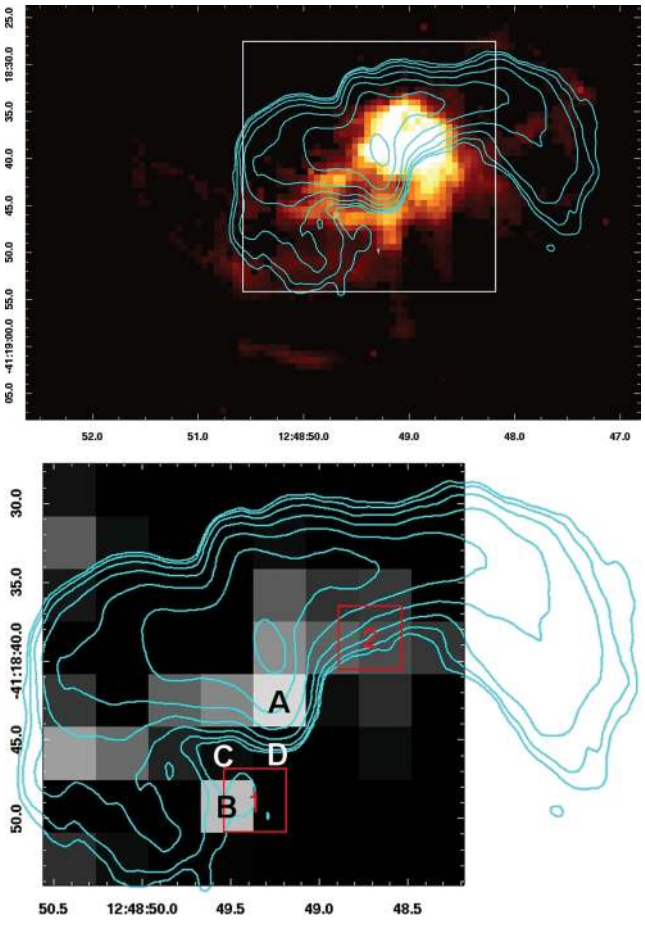

Figure 11. The spatial distribution of the 10^6-K gas. Top panel: the [N II] λ6583 emission, overlaid with VLA 5-GHz radio contours (Taylor et al. 2007). The white box indicates the region, where we have our deepest observations. Bottom panel: this region binned on a 5 by 5 fibre basis, showing the residual flux at the position of the [Fe X] λ6374 emission across the field of view. The brightest bins are regions of highest flux. The spectra from bins A–D are shown in Fig. 12. For comparison, boxes 1 and 2 are marked in red.

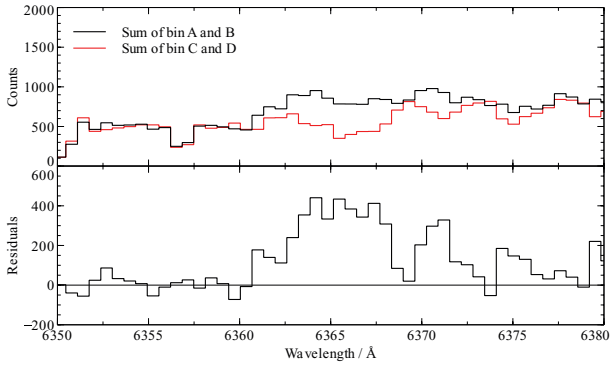

Figure 12. A comparison of the spectra from four of the regions marked on Fig. 11. The spectra have been continuum subtracted, and the [O I] λ6363 object emission line and the two sky lines to the left-hand side of the oxygen line have been fitted and removed. The bottom panel shows the residuals between the two spectra.

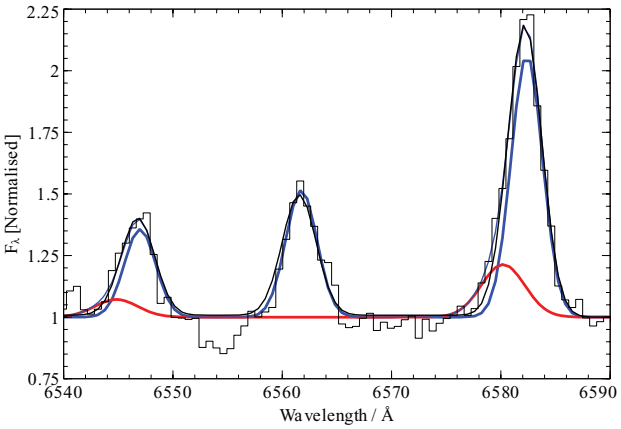

Figure 13. A two-component fit to the Hα and [N II] emission from box 1. There is evidence for a slightly blueshifted component to these lines with a blueshifted velocity of $\sim$140 km s^{-1}. This is smaller than the velocity shift seen in the [Fe X] λ6374 emission line of $\sim$230 km s^{-1}.

The cooling rates are derived for cooling without heating and so may be lower than stated; they may also vary across the temperature range probed. Investigations of the quantity of molecular gas and dust and of recent star formation in these objects may help constrain the quantity of cooling, to very low temperatures, that we expect. A much lower cooling rate may provide an explanation for the lack of [Fe XIV] λ5303 and [Ni XV] λ6702 emission we see; however, the calcium lines should originate from a temperature range that has been directly observed from measurements of the Fe XVII line ratios, so the lack of this emission is not easily understood.

The Centaurus cluster has very high metallicities, which peak at a radius of 20 kpc and then decline towards the nucleus (Sanders & Fabian 2006a). This enhancement and decline in the metallicities are reproduced using both *XMM–Newton*, *Chandra* CCD observations and *XMM–Newton* RGS observations. An off-centre abundance peak with a depression in abundance towards the centre of clusters and groups is often observed in objects with cool cores (see e.g. De Grandi & Molendi 2001; Rasmussen & Ponman 2007 and De Grandi & Molendi 2009).

There are a number of biases and uncertainties in abundance measurements from spectral modelling. Inaccuracies in modelling the temperature structure of galaxy clusters can introduce an 'Fe bias' (Buote 2000). Here the measured Fe abundance is lower than the actual value due to fitting a multiphase gas with single or only a couple of temperature components. The opposite effect, an 'inverse Fe bias', is also seen in cool core clusters when a single temperature model is fitted to a multiphase plasma with temperatures between 2–4 keV (Rasia et al. 2008). In the case of the Centaurus cluster, the high spectral resolution of *XMM–Newton* RGS allows the temperature to be constrained with line-strength ratios giving a more robust check on the temperature components of the models (Sanders et al. 2008).

Sedimentation in the centre of galaxy clusters (Fabian & Pringle 1977) can cause the metal abundances to rise and could be reversed by the effects of thermal diffusion (Shtykovskiy & Gilfanov 2010). Neglecting the effects of resonance scattering also underestimates the abundances of metals in clusters. This effect is at most 10 per cent, so cannot fully explain the central abundance dips observed in galaxy clusters (Sanders & Fabian 2006b). The drop in abundances in the Centaurus cluster may be explained with a complex model involving three temperature components and additional absorption; however, the errors on the inner-most radial bins become sufficiently large that it is impossible to tell if the drop is real or not (Fabian et al. 2005).

A major contributor to a central abundance drop must be depletion on dust. The central few kpc of the hot gas will be dominated by stellar mass-loss, in which most metals are bound in dust grains. They will slowly be introduced into the hot phase by sputtering, at a rate dependent on the grain size (Draine & Salpeter 1979; Barlow 1978). Much iron, however, could be injected into the hot phase through Type Ia supernovae.

Calcium is one of the most depleted of all refractory elements in the presence of dust (Field 1974; Spitzer & Jenkins 1975; Cowie & Songaila 1986), with depletions of 10^{-4} relative to solar abundance typical in dense clouds. NGC 4696 hosts a huge dust lane, which almost completely encircles the core and spirals out to the north-east, tracing the morphology of the Hα filaments. The X-ray absorption column density is also highest in the same region (Crawford et al. 2005). It has moreover a large quantity of infrared-emitting dust in its nucleus (Goudfrooij & de Jong 1995; Kaneda et al. 2007). Kaneda et al. (2007) show from the *Spitzer* Multiband Imaging Photometer (MIPS) 24-μm surface brightness profiles that the dust emission increases steeply in the inner 30 arcsec (6.3 kpc), a region slightly larger than our field of view and where we observe the metallicity drop.

The cumulative gas mass obtained from the X-ray-emitting hydrogen density profile of Graham et al. (2006) in the inner 30 arcsec or 6.3 kpc (10 arcsec, 2.1 kpc) is $9.4 \times 10^8\,M_\odot$ ($9.2 \times 10^7\,M_\odot$). Assuming a dust-to-gas ratio similar to our Galaxy (Crawford et al. 2005; Edge et al. 2010), we get a total dust mass of $9.4 \times 10^6\,M_\odot$ ($9.2 \times 10^5\,M_\odot$). The dust mass estimated by Goudfrooij & de Jong (1995) using the *Infrared Astronomical Satellite* (*IRAS*) is $4.7 \times 10^6\,M_\odot$ and the *Spitzer* MIPS result from Kaneda et al. (2007) is $4.2 \times 10^5\,M_\odot$. These values are considered to be lower limits to the dust mass as the instruments are insensitive to very cold dust and imply that the inner interstellar medium in NGC 4696 is highly deficient in refractory elements.

A number of cool core clusters have been found to be deficient in calcium in the warm (10^4-K) emission-line nebulae, where [Ca II] and [Ca V] emission lines would be expected (Donahue & Voit 1993; Ferland 1993). Our spectra of NGC 4696 are consistent with this, since they show no evidence for [Ca II] or [Ca V] emission in the inner regions of NGC 4696.

These results indicate that NGC 4696 is deficient in gas-phase calcium at temperatures below $\sim 5 \times 10^6$ K. The lack of this warm and intermediate-temperature gas phase in the inner 20 arcsec implies that the calcium in dust has never been part of the hot ICM and was probably introduced in dusty stellar mass-loss.

The high calcium abundance in the hot gas, discovered by Sanders & Fabian (2006a), has its greatest contribution from the hot 4-keV emission (the contribution from the best fit to the lower temperature component, 0.5 keV, is negligible). This is consistent with the dust being sputtered by the hotter gas at large radii ($\geq$ few kpc), where there are also no shielding 'cold' filaments.

5 CONCLUSION

We report the detection of [Fe X] λ6374 coronal line emission in NGC 4696. This emission probes temperatures of 10^6 K and is the first detection of intermediate-temperature gas in this object. We fail to detect emission from coronal lines of higher temperature gas, including those of [Ca XV], which probe gas of 5×10^6 K and which we had expected to detect due to the high abundance of calcium in the hot X-ray-emitting gas.

We conclude that calcium is likely to be depleted in the dusty central regions of NGC 4696. This is consistent with our apparent lack of [Ca V] and [Ca II] ions, which probe lower temperature gas, and with the negligible contribution to the abundance in the hot gas of the lower temperature 0.5-keV calcium lines. The dust in the central region of the galaxy is likely due to stellar mass-loss and has survived as dust grains due to the shelter of surrounding cooler gas. The abundance of calcium is higher in the outer 4-keV ICM, since dust is sputtered there, where the dust is less protected by the cooler surroundings and the cold filaments. Deeper, high-resolution X-ray observations, which better constrain the central abundances of Fe, Si, Ca and Ne, would help to distinguish between the processes that contribute to the metal abundance.

There is now strong evidence to show that the central galaxies in many cool core clusters are playing host to large quantities of dust and cool gas (see e.g. McNamara & O'Connell 1992; Edge et al. 2010). Donahue & Voit (1993) have also shown that the [Ca II] doublet is much weaker than expected in a sample of BCGs. Similarly, they conclude that calcium is most likely depleted into dust grains in their sample.

The cooling rate inferred by the [Fe X] λ6374 emission is large ($20\,M_\odot\,yr^{-1}$ in a spatial region of 20 arcsec^2) compared with that determined from other lines in the optical and X-ray spectrum. This and the apparent lack of [Fe XIV] λ5303 and [Ni XV] λ6702 emission rules out a steady cooling flow from the 10^7-K gas in this object. Some gas may, however, be cooling non-radiatively, for example, by mixing with the colder gas. The strength of the [Fe X] emission suggests that the 10^6-K gas is being heated rather than condensing out of the hot ISM.

ACKNOWLEDGMENTS

REAC acknowledges STFC for financial support. ACF thanks the Royal Society. GJF gratefully acknowledges support by NSF (0607028 and 0908877) and NASA (07-ATFP07-0124). REAC would also like to thank Rob Sharp, for allowing to use his IFU IDL routines, and Ryan Cooke, Paul Hewett and Ben Johnson for help and valuable discussions.

This research has made use of the NASA/IPAC Extragalactic Data base (NED), which is operated by the Jet Propulsion Laboratory, California Institute of Technology, under contract with the National Aeronautics and Space Administration.

The STARLIGHT project is supported by the Brazilian agencies CNPq, CAPES and FAPESP and by the France-Brazil CAPES/Cofecub programme.

The data published in this paper have been reduced using VIPGI, designed by the VIMOS Consortium and developed by INAF Milano.

The figures in this paper were produced using VEUSZ.[2]

REFERENCES

Amico P., Bagnulo S., Dumas C., Izzo C., Marconi G., Melo C., 2008, in Kaufer A., Kerber F., eds, Proc. ESO Workshop held in Garching, Germany, 23–26 January 2007, The 2007 ESO Instrument Calibration Workshop. Springer-Verlag, Berlin/Heidelberg, p. 279

Anders E., Grevesse N., 1989, Geochim. Cosmochim. Acta, 53, 197

Anton K., Wagner S., Appenzeller I., 1991, A&A, 246, L51

Barlow M. J., 1978, MNRAS, 183, 367

Bregman J. N., Fabian A. C., Miller E. D., Irwin J. A., 2006, ApJ, 642, 746

Bruzual G., Charlot S., 2003, MNRAS, 344, 1000 (BC03)

Buote D. A., 2000, MNRAS, 311, 176

[2] http://home.gna.org/veusz/

Cid Fernandes R., Mateus A., Sodré L., Stasińska G., Gomes J. M., 2005, MNRAS, 358, 363
Cid Fernandes R. et al., 2009, RMxAA, 35, 127
Cowie L. L., 1981, in Giacconi R., ed., Astrophysics and Space Science Library, Vol. 87. X-ray Astronomy with the Einstein Satellite. Riedel, Dordrecht, p. 227
Cowie L. L., Songaila A., 1986, ARA&A, 24, 499
Crawford C. S., Hatch N. A., Fabian A. C., Sanders J. S., 2005, MNRAS, 363, 216
De Grandi S., Molendi S., 2001, ApJ, 551, 153
De Grandi S., Molendi S., 2009, A&A, 508, 565
Donahue M., Stocke J. T., 1994, ApJ, 422, 459
Donahue M., Voit G. M., 1993, ApJ, 414, L17
Draine B. T., Salpeter E. E., 1979, ApJ, 231, 77
Edge A. C. et al., 2010, preprint (arXiv:1005.1211)
Fabian A. C., Pringle J. E., 1977, MNRAS, 181, 5P
Fabian A. C., Sanders J. S., Taylor G. B., Allen S. W., 2005, MNRAS, 360, L20
Ferguson J. W., Korista K. T., Baldwin J. A., Ferland G. J., 1997, ApJ, 487, 122
Ferland G. J., 1993, in Beckman J., Colina L., Netzer H., eds, The Nearest Active Galaxies. Consejo Superior de Investigaciones, Madrid, p. 75
Field G. B., 1974, ApJ, 187, 453
Goudfrooij P., de Jong T., 1995, A&A, 298, 784
Graham J., Fabian A. C., Sanders J. S., Morris R. G., 2006, MNRAS, 368, 1369
Graney C. M., Sarazin C. L., 1990, ApJ, 364, 561
Heckman T. M., Baum S. A., van Breugel W. J. M., McCarthy P., 1989, ApJ, 338, 48
Hu E. M., Cowie L. L., Wang Z., 1985, ApJS, 59, 447
Kaneda H., Onaka T., Kitayama T., Okada Y., Sakon I., 2007, PASJ, 59, 107
LeFevre O. et al., 2003, in Iye M., Moorwood A. F. M., eds, SPIE Conf. Ser. Vol. 4841, SPIE, Bellingham, p. 1670
McNamara B. R., O'Connell R. W., 1992, ApJ, 393, 579
McNamara B. R. et al., 2006, ApJ, 648, 164
Markwardt C. B., 2009, in Bohlender D. A., Durand D., Dowler P., eds, ASP Conf. Ser. Vol. 411, Astronomical Data Analysis Software and Systems XVIII. Astron. Soc. Pac., San Francisco, p. 251
Mazzalay X., Rodríguez-Ardila A., Komossa S., 2010, MNRAS, 405, 1315
Moré J. J., 1978, The Levenberg-Marquardt Algorithm: Implementation and Theory, Springer-Verlag, Berlin/Heidelberg
Mullaney J. R., Ward M. J., Done C., Ferland G. J., Schurch N., 2009, MNRAS, 394, L16
Oegerle W. R., Cowie L., Davidsen A., Hu E., Hutchings J., Murphy E., Sembach K., Woodgate B., 2001, ApJ, 560, 187
Osterbrock D. E., Ferland G. J., 2006, Astrophysics of Gaseous Nebulae and Active Galactic Nuclei. University Science Books, Mill Valley, CA
Peterson J. R., Fabian A. C., 2006, Phys. Rep., 427, 1
Rasia E., Mazzotta P., Bourdin H., Borgani S., Tornatore L., Ettori S., Dolag K., Moscardini L., 2008, ApJ, 674, 728
Rasmussen J., Ponman T. J., 2007, MNRAS, 380, 1554
Sabra B. M., Shields J. C., Filippenko A. V., 2000, ApJ, 545, 157
Sanders J. S., Fabian A. C., 2002, MNRAS, 331, 273
Sanders J. S., Fabian A. C., 2006a, MNRAS, 371, 1483
Sanders J. S., Fabian A. C., 2006b, MNRAS, 370, 63
Sanders J. S., Fabian A. C., Allen S. W., Morris R. G., Graham J., Johnstone R. M., 2008, MNRAS, 385, 1186
Sarazin C. L., Graney C. M., 1991, ApJ, 375, 532
Scodeggio M. et al., 2005, PASP, 117, 1284
Shields J. C., Filippenko A. V., 1992, AJ, 103, 1443
Shtykovskiy P., Gilfanov M., 2010, MNRAS, 401, 1360
Sparks W. B., Macchetto F., Golombek D., 1989, ApJ, 345, 153
Sparks W. B., Pringle J. E., Donahue M., Carswell R., Voit M., Cracraft M., Martin R. G., 2009, ApJ, 704, L20
Spitzer L., Jr, Jenkins E. B., 1975, ARA&A, 13, 133
Taylor G. B., Gugliucci N. E., Fabian A. C., Sanders J. S., Gentile G., Allen S. W., 2006, MNRAS, 368, 1500
Taylor G. B., Fabian A. C., Gentile G., Allen S. W., Crawford C., Sanders J. S., 2007, MNRAS, 382, 67
Voit G. M., Donahue M., Slavin J. D., 1994, ApJS, 95, 87
Yan L., Cohen J. G., 1995, ApJ, 454, 44
Zanichelli A. et al., 2005, PASP, 117, 1271

This paper has been typeset from a TEX/LATEX file prepared by the author.